nature nanotechnology

Article

https://doi.org/10.1038/s41565-023-01336-z

Chiral antiferromagnetic Josephson junctions as spin-triplet supercurrent spin valves and d.c. SQUIDs

Received: 19 November 2021

Accepted: 31 January 2023

Published online: 30 March 2023

Check for updates

Kun-Rok Jeon[1,2] ✉, Binoy Krishna Hazra[1], Jae-Keun Kim[1], Jae-Chun Jeon[1], Hyeon Han[1], Holger L. Meyerheim[1], Takis Kontos[3], Audrey Cottet[3] ✉ & Stuart S. P. Parkin[1] ✉

Spin-triplet supercurrent spin valves are of practical importance for the realization of superconducting spintronic logic circuits. In ferromagnetic Josephson junctions, the magnetic-field-controlled non-collinearity between the spin-mixer and spin-rotator magnetizations switches the spin-polarized triplet supercurrents on and off. Here we report an antiferromagnetic equivalent of such spin-triplet supercurrent spin valves in chiral antiferromagnetic Josephson junctions as well as a direct-current superconducting quantum interference device. We employ the topological chiral antiferromagnet Mn_3Ge, in which the Berry curvature of the band structure produces fictitious magnetic fields, and the non-collinear atomic-scale spin arrangement accommodates triplet Cooper pairing over long distances (>150 nm). We theoretically verify the observed supercurrent spin-valve behaviours under a small magnetic field of <2 mT for current-biased junctions and the direct-current superconducting quantum interference device functionality. Our calculations reproduce the observed hysteretic field interference of the Josephson critical current and link these to the magnetic-field-modulated antiferromagnetic texture that alters the Berry curvature. Our work employs band topology to control the pairing amplitude of spin-triplet Cooper pairs in a single chiral antiferromagnet.

Intensive studies in coupling superconducting condensate state with magnetic-exchange spin splitting have opened up a research field of superconducting spintronics[1–3], which promises to realize dissipationless spin-based logic and memory technologies. Of particular relevance in this research is the theoretical prediction[4–7] and experimental verification[8–12] that spin-polarized triplet pairing states can be created via spin-mixing and spin-rotation processes (for example, non-collinear exchange fields[4–6,8–10] in real space and/or spin–orbit fields[7,11,12] in reciprocal/*k* space) at proximity-engineered superconductor/ferromagnet (FM) interfaces[1–12]. With these advances, the field of superconducting spintronics involving spin-polarized triplet Cooper pairs[1–3] can answer two practical aspects: how to efficiently generate such triplet pairs and how to tune them in a controllable manner. Yet, as previously pointed out[4,13,14], fulfilling these two requirements at the same time seems challenging because the preconfigured robust non-collinearity of spin-mixer and spin-rotator magnetizations for a higher singlet-to-triplet pair conversion makes it difficult to control by an external stimulus.

The active and reversible control of spin-polarized triplet supercurrents has so far been mostly achieved in ferromagnetic Josephson

[1]Max Planck Institute of Microstructure Physics, Halle (Saale), Germany. [2]Department of Physics, Chung-Ang University (CAU), Seoul, Republic of Korea. [3]Laboratoire de Physique de l'Ecole normale supérieure, ENS, Université PSL, CNRS, Sorbonne Université, Université de Paris, Paris, France. ✉e-mail: jeonkunrok@gmail.com; audrey.cottet@physics.ens.fr; stuart.parkin@mpi-halle.mpg.de

junctions (JJs)[13,14], where at least three FMs constitute a Josephson barrier whose relative magnetization directions, and therefore the non-collinearity, can be controlled by external magnetic fields[4,13,14]. This has led to the so-called spin-triplet supercurrent spin valve[4,13,14], in which the proximity-created spin-polarized triplet supercurrents can be switched on and off. However, the fabrication of such ferromagnetic spin-triplet JJs[13,14] requires delicate interface engineering, for instance, electronic energy band matching between neighbouring layers, selectivity in coercive fields of the spin-mixer and spin-rotator FMs and circumventing the out-of-plane (OOP) component of stray magnetic fields.

In this work, we demonstrate an antiferromagnetic analogue of the spin-triplet supercurrent spin-valve effect[4,13,14] via the use of a single topological chiral antiferromagnet (AFM) Mn_3Ge (refs. 15–17), which—with its lack of stray fields—can be highly advantageous for developing superconducting spintronic logic circuits[1]. The noteworthy aspect of Mn_3Ge is that its non-collinear triangular antiferromagnetic spin arrangement[15–17] in real space (Fig. 1a,b) and the fictitious magnetic fields derived from Berry curvature[18,19] in k space, which are robust to low temperature T (refs. 15–17,20), facilitate the spin-mixing and spin-rotation processes[1–12] required for singlet-to-triplet pair conversion. This enables, as shown in our recent experiment[20], the proximity generation of long-range triplet supercurrents through the single chiral antiferromagnetic Josephson barrier.

Chiral antiferromagnetic spin-triplet JJs

Our focus of the present study is on the Berry-curvature-driven fictitious fields[18,19] that play an effective role in converting spin-unpolarized singlet Cooper pairs ($S = 0$) to form long-range triplets ($S = 1$) in the topological chiral AFM[20]. Note that how non-collinear six spins on a kagome bilayer[15–17], constituting a cluster magnetic octupole, are arranged in real space (equivalently, how time-reversal symmetry is broken) determines the Berry curvature profile[18,19] in k space. So, an external magnetic field $\mu_0 H_\perp$ applied perpendicular to the kagome plane tilts the overall antiferromagnetic spin arrangement to a certain extent to the field direction (Fig. 1a,b) and subsequently changes the associated Berry curvature[18] around the Fermi energy and the resulting fictitious fields[19], as theoretically calculated[21,22]. This offers, as shown below, a radically different approach to control the pair amplitude of triplets by applying an extremely small magnetic field (<2 mT). Our k-space Berry curvature approach is conceptually different from very recent works on controlling spin-triplet critical currents in a single FM with magnetic vortex[23] and domain wall[24], both of which focus on the real-space magnetic texturing across the FM Josephson barrier.

We carry out proof-of-concept experiments based on Nb/Mn_3Ge/Nb lateral JJs[20] (Fig. 1c). In particular, the edge-to-edge separation distance d_s of the adjacent superconducting Nb electrodes through an epitaxial thin film of the triangular chiral AFM Mn_3Ge (Fig. 1a,b) is chosen to be comparable with or larger than the characteristic decay length $\xi_{\text{triplet}}^{Mn_3Ge} = 157$–$178$ nm (at $T = 2$ K; Extended Data Fig. 1) of spin-polarized triplet supercurrents[20]. Conventional wisdom is that the spin-unpolarized singlets ($S = 0$) are mostly exchange field filtered within a few nanometres[1–12] and the surviving spin-polarized triplets ($S = 1$, $m_s = \pm 1$), which are immune to magnetic exchange fields[1–12,25], finally mediate the long-range Josephson coupling. The mechanism for producing triplet Cooper pairs is a priori different in our case and we call this chiral antiferromagnetic spin-triplet JJs.

Hysteretic out-of-kagome-plane magnetic-field interference patterns

Figure 1c,d shows the typical magnetic-field interference pattern of Josephson critical current $I_c(\mu_0 H_\perp)$ for the $d_s = 199$ nm JJ at $T = 2$ K. Here $\mu_0 H_\perp$ is applied along [0001] and thus perpendicular to the kagome plane of our single-phase hexagonal $D0_{19}$-Mn_3Ge(0001) layer (Fig. 1a,b and Methods). There exist two distinctively different features from the $I_c(\mu_0 H_\perp)$ interference pattern of our prior $d_s \leq 115$ nm JJs[20]. First, the zero-order maximum of I_c appears 0.5–1.0 mT away from the zero field ($\mu_0 H_\perp = 0$) and it is clearly hysteretic (Fig. 1e). As our single-phase $D0_{19}$-Mn_3Ge(0001) has a vanishingly small spontaneous magnetization (≤11 emu c.c.$^{-1}$ at 2 K)[20] in the kagome plane[15–17,20], we ascribe this hysteretic $I_c(\mu_0 H_\perp)$ to the OOP-magnetic-field-modulated Berry curvature, as discussed later. Second, we obtain the characteristic $I_c(\mu_0 H_\perp)$ oscillation with clear minima for the $d_s = 199$ nm JJ (Fig. 1d), indicating the transverse uniformity of I_c across the whole Mn_3Ge barrier and its coherent spatial quantum interference[26]. This improved magnetic-field interference in a longer JJ is probably due to the reduced effective edge roughness (several nanometres) of Nb electrodes relative to d_s, given that the single crystallinity and surface morphology of previous[20] and current $D0_{19}$-Mn_3Ge(0001) layers are not fundamentally different (Extended Data Fig. 2).

Our theory, considering a chirality-dependent phase $Qwd_s\frac{J\delta M}{\hbar v_F}\tau$ arising from the antiferromagnetic spin texture of Mn_3Ge (Supplementary Section 1 provides the full details), anticipates the unique hysteretic Fraunhofer pattern and reproduces the overall $I_c(\mu_0 H_\perp)$ data (Fig. 1d, solid lines):

$$I_c(\mu_0 H_\perp) = I_0\left(\left(\sum_\tau\left(1+\tau\frac{2\chi\gamma}{\gamma^2+\chi^2}\right)\sin\left(d_s\frac{2JM_0}{\hbar v_F}\tau\right)\operatorname{sinc}\left(\pi\frac{\Phi_{JJ}}{\Phi_0}+Qwd_s\frac{J\delta M}{\hbar v_F}\tau\right)\right)^2\right.$$
$$\left.+\left(\sum_\tau\left(1+\tau\frac{2\chi\gamma}{\gamma^2+\chi^2}\right)\cos\left(d_s\frac{2JM_0}{\hbar v_F}\tau\right)\operatorname{sinc}\left(\pi\frac{\Phi_{JJ}}{\Phi_0}+Qwd_s\frac{J\delta M}{\hbar v_F}\tau\right)\right)^2\right)^{\frac{1}{2}}.$$

Here Q, δM and J are the inverse antiferromagnetic domain size, amplitude of the inhomogeneous part and exchange interaction of the antiferromagnetic spin texture of Mn_3Ge, respectively; τ is the chirality index (±1); γ represents the transparency at the Nb/Mn_3Ge interface; and χ describes the chirality dependence of the Mn_3Ge barrier. Here $\hbar$ is the reduced Planck constant and v_F is the Fermi velocity of Mn_3Ge. Also, $\Phi_{JJ} = \mu_0 H_\perp A_{JJ}^{\text{eff}}$ and $A_{JJ}^{\text{eff}} = (2\lambda_L + d_s)w$ is the effective junction area of magnetic flux penetration (Fig. 1d, bottom inset), λ_L is the London penetration depth (130 nm at 2 K)[27] of 50-nm-thick Nb electrodes, w is the width of the Mn_3Ge barrier and $\Phi_0 = \frac{h}{2e} = 2.07\times10^{-15}$ T m^2 is the magnetic flux quantum. From theoretical reproduction, we get $w \approx 1.1$ μm, close to the actual width of our JJ (Fig. 1c), and $\left|Qwd_s\frac{J\delta M}{\hbar v_F}\tau\right| = 0.2$ (Supplementary Section 2 provides a quantitative analysis).

Spin-triplet supercurrent spin valves

We now measure the time-averaged voltage V as a function of $\mu_0 H_\perp$ for the d.c. current I-biased JJs with $d_s = 28$–199 nm (Fig. 2a–d), from which, especially at $I \approx I_c(\mu_0 H_\perp = 0)$, one can straightforwardly see how the supercurrent spin-valve behaviour evolves as a function of d_s. All the JJs in the superconducting state ($T = 2$ K) reveal asymmetric $V(\mu_0 H_\perp)$ curves with respect to $\mu_0 H_\perp = 0$ and their asymmetry is rigorously inverted when reversing the $\mu_0 H_\perp$ sweep direction. Note that since this asymmetric hysteretic behaviour disappears when the junctions are in the normal state ($T = 8$ K), it is necessarily connected to superconductivity induced in the chiral AFM leading to the Josephson supercurrent. With increasing d_s, the centre-to-centre offset $\Delta\mu_0 H_\perp$ between the sweep-up and sweep-down $V(\mu_0 H_\perp)$ curves progressively broaden from 0.1 to 1.5 mT and the consequent asymmetric hysteresis becomes more evident. On reaching $d_s = 199$ nm (Fig. 2d), comparable with or larger than $\xi_{\text{triplet}}^{Mn_3Ge}$ (157–178 nm; Extended Data Fig. 1) over which the proximity-created spin triplets can primarily mediate the long-range Josephson coupling[1–12], the complete antiferromagnetic analogue of the spin-triplet supercurrent spin valve[4,13,14] is established in our chiral antiferromagnetic JJ. The applied $\mu_0 H_\perp \leq 2.0$ mT here to turn the Josephson supercurrent on and off (Fig. 2d) is intriguingly one order of magnitude smaller than that typically required for ferromagnetic spin-triplet JJs[13,14], where one should apply a magnetic field larger than the coercive field of the free spin-rotator FM_2 (for example, a few tens

https://doi.org/10.1038/s41565-023-01336-z

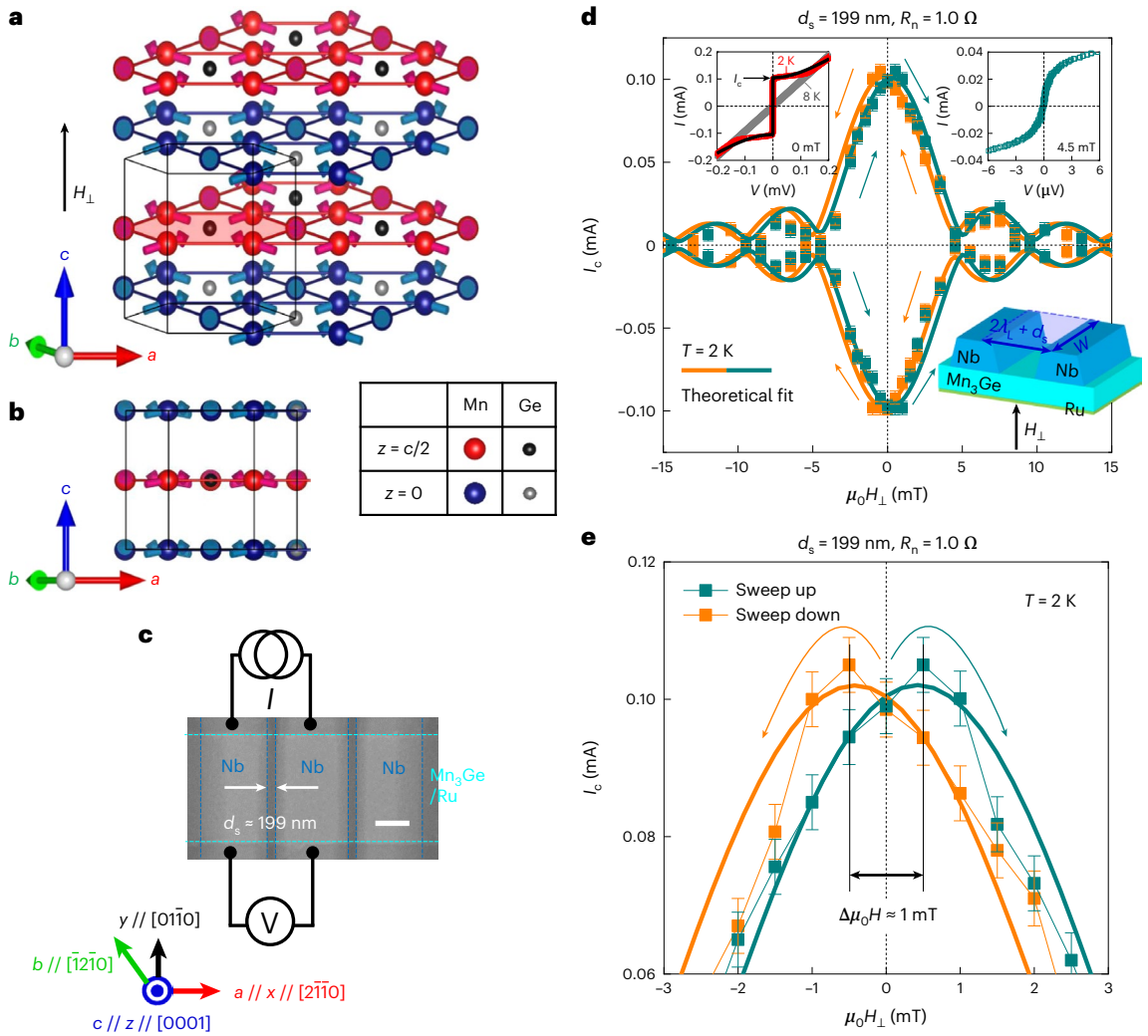

Fig. 1 | Hysteretic magnetic-field interference pattern of chiral antiferromagnetic spin-triplet JJs. a,**b**, Probable 120° chiral antiferromagnetic configurations and crystal structure of $D0_{19}$-Mn_3Ge(0001) canted out of the kagome plane under a perpendicular magnetic field $\mu_0H_\perp$ (perpendicular to the a–b plane). Two layers of Mn and Ge atoms are stacked along the c axis (parallel to the z axis), where blue and grey (red and black circles) represent Mn and Ge atoms lying in the $z = 0$ ($z = c/2$) plane, respectively. **c**, Scanning electron micrograph of the fabricated Nb/Mn_3Ge/Nb lateral JJs. Note that the 5-nm-ultrathin Ru underlayer acts as a buffer layer (Methods). Scale bar, 0.5 μm. **d**, Josephson critical current I_c versus $\mu_0H_\perp$ plot for the $d_s = 199$ nm Nb/Mn_3Ge/Nb JJ, taken at $T = 2$ K. Here $\mu_0H_\perp$ is applied perpendicular to the kagome (interface) plane of the Mn_3Ge barrier (Nb electrodes) (bottom inset). The top-left inset displays the zero-field I–V curve above (8 K) and below (2 K) the superconducting transition of the JJ. The top-right inset shows the I–V curve near the zero-order minimum of $I_c(\mu_0H_\perp)$. The solid lines correspond to our theoretical reproduction that takes both real-space magnetic texture (under an OOP magnetic field) and the k-space Weyl nodes into account (Supplementary Section 1). **e**, Magnified $I_c(\mu_0H_\perp)$ plot around $\mu_0H_\perp = 0$ where asymmetric hysteretic $I_c(\mu_0H_\perp)$ interference with the zero-order maximum-to-maximum offset $\Delta\mu_0H_\perp = 1.0$ mT is evident. The error bars in **d** and **e** represent the standard deviation.

of millitesla even for soft FM Ni_8Fe_2)[13] to change its magnetization direction relative to the pinned spin-mixer FM_1, providing a beneficial route for controlling the pair amplitude of the spin triplets.

Supercurrent spin valve and 0-to-π phase shift in a d.c. SQUID

By taking advantage of this low-field spin-triplet supercurrent spin valve, we next fabricate a direct-current superconducting quantum interference device (d.c. SQUID) to showcase its potential as an on-chip local probe[28] of out-of-kagome-plane magnetic moments of chiral AFMs with high sensitivity. Note that because the active superconducting loop of our SQUID (Fig. 3a,b and Methods) contains two chiral antiferromagnetic spin-triplet JJs of $d_s = 172$ and 179 nm ($\geq \xi_{triplet}^{Mn_3Ge}$) that are laterally connected through the single layer of $D0_{19}$-Mn_3Ge(0001), the SQUID action of this device is available only when the superconducting Nb electrodes are Josephson coupled via spin-triplet Cooper pairs[24,29]. From the zero-field current–voltage (I–V) curve of the fabricated SQUID (Fig. 3c), we find that the total critical current I_c^{tot} is approximately twice the I_c value of a single JJ with similar d_s (Extended Data Fig. 1). This matches the standard theory[26] of a d.c. SQUID comprising two overdamped JJs[20,26] with a low resistance–capacitance product, that is,

$$I_c^{tot}(\mu_0H_\perp) = \sqrt{(I_{c1} - I_{c2})^2 + 4I_{c1}I_{c2}\left(\cos\left(\pi\frac{\Phi_{SQUID}}{\Phi_0} + \left(\frac{\varphi_1 + \varphi_2}{2}\right)\right)\right)^2}.$$

Here we assume a small self-inductance of the SQUID loop for simplicity and consider the low-field regime ($\Phi_{JJ} \ll \Phi_0$) such that the $I_c^{tot}(\mu_0H_\perp)$ curve mostly reflects the SQUID characteristics. Here I_{c1} (I_{c2}) and φ_1 (φ_2) are the zero-field Josephson critical current and intrinsic phase difference[30] for the first (second) JJ of the SQUID, respectively. Also, $\Phi_{SQUID} = \mu_0H_\perp A_{SQUID}^{eff}$ is the magnetic flux threading the SQUID loop

https://doi.org/10.1038/s41565-023-01336-z

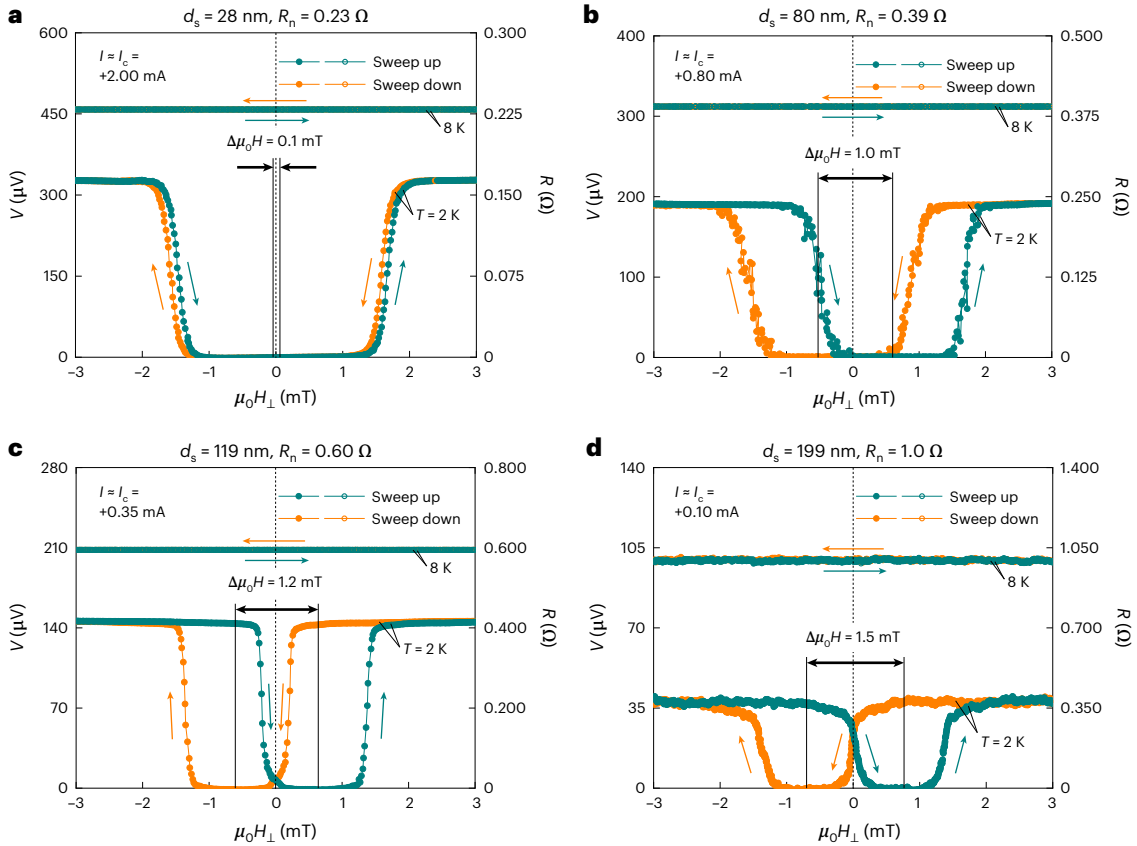

Fig. 2 | Supercurrent spin-valve effect in chiral antiferromagnetic spin-triplet JJs. a–d, Time-averaged voltage V as a function of external magnetic field $\mu_0 H_\perp$ for the d.c. current I-biased Nb/Mn_3Ge/Nb JJs with different barrier spacing d_s values of 28 nm (**a**), 80 nm (**b**), 119 nm (**c**) and 199 nm (**d**), taken above (8 K) and below (2 K) the superconducting transition of the JJs. In these measurements, we apply fixed I that is similar to the zero-field Josephson critical current $I_c(\mu_0 H_\perp = 0)$ of each JJ to straightforwardly visualize how the supercurrent spin-valve effect depends on d_s. Note that $\mu_0 H_\perp$ (≤|3 mT|) is applied perpendicular to the kagome plane of the Mn_3Ge barrier, and the JJ data in **a**–**c** are identical to what we used for our prior study[20].

given by $\mu_0 H_\perp$ and $A^{\mathrm{eff}}_{\mathrm{SQUID}} = (2\lambda_L + L_x)(2\lambda_L + L_y)$ is the effective SQUID area (Fig. 3b). Note that for $\mu_0 H_\perp = 0$, $I_c^{\mathrm{tot}} = I_{c1} + I_{c2}$.

Most importantly, the low-field supercurrent spin-valve functionality, that is, the active modulation of Josephson coupling strength as well as the ground-state phase difference, is successfully implemented in the SQUID oscillation (Fig. 3d–f). To the best of our knowledge, only a recent work utilizing multiple FMs has succeeded in the controllable switching between 0- and π-phase states of the ferromagnetic spin-triplet JJs embedded in a d.c. SQUID[29]. As summarized in Fig. 3g, the implemented spin-valve amplitude $\Delta R = R_{\mathrm{high}} - R_{\mathrm{low}}$ increases with increasing I and achieves the maximum value at $I \approx I_c^{\mathrm{tot}}(\mu_0 H_\perp = 0)$, followed by a strong drop for larger I. Especially for $I \lesssim I_c^{\mathrm{tot}}(\mu_0 H_\perp = 0)$, we obtain an infinite spin-valve magnetoresistance $\mathrm{MR} = \frac{\Delta R}{R_{\mathrm{low}}} \to \infty$ by definition with rigorous switching between quasiparticle currents and supercurrents (Fig. 3d,g). This demonstration of the SQUID spin-valve oscillation can be used to devise a phase-resolved and magnetization-component-specific detector of antiferromagnetic domain walls, which remains a major challenge in the research field of AFM spintronics[28].

For the I-biased SQUID of two overdamped JJs in the limit of small self-inductance and in the low-field limit ($\Phi_{\mathrm{JJ}} \ll \Phi_0$), the conversion of a magnetic flux into V modulation can be approximated by[26]

$$V(\mu_0 H_\perp, I) = \frac{R_{n1}R_{n2}}{R_{n1}+R_{n2}}\sqrt{(I)^2 - \left(I_c^{\mathrm{tot}}\cos\left(\pi\frac{\Phi_{\mathrm{SQUID}}}{\Phi_0} + \left(\frac{\varphi_1+\varphi_2}{2}\right)\right)\right)^2},$$

where R_{n1} (R_{n2}) is the normal-state zero-bias resistance of the first (second) JJ. From the measured $V(\mu_0 H_\perp, I \geq I_c^{\mathrm{tot}})$ oscillation with a period of $\mu_0 H_{\mathrm{osc}}$ = 0.16–0.24 mT (Fig. 3d–f and Extended Data Fig. 3) and using the relationship $\mu_0 H_{\mathrm{osc}} = \frac{\Phi_0}{A^{\mathrm{eff}}_{\mathrm{SQUID}}}$, we obtain $A^{\mathrm{eff}}_{\mathrm{SQUID}}$ = 9–13 μm². This value is 2–3 times larger than the geometrical area of the SQUID loop ($(2\lambda_L + L_x)(2\lambda_L + L_y)$ = 4.1 μm²), which we attribute to a flux-focusing effect. Note that if the width of the SQUID loop is much larger than λ_L, the flux-focusing effect comes into play and effectively widens the SQUID area to be $L_x^{\mathrm{ctc}} L_y^{\mathrm{ctc}} \approx 11\ \mu\mathrm{m}^2$ (Fig. 3b), indicating the reliable performance of our SQUID. Here $L_{x,y}^{\mathrm{ctc}}$ is the centre-to-centre spacing between the tracks defining the two opposite sides of the SQUID.

Interestingly, from a comparison of the sweep-up and sweep-down $V_{\mathrm{SQUID}}(\mu_0 H_\perp)$ data (Fig. 3f and Extended Data Fig. 4), a finite phase shift of $\varphi_1 + \varphi_2 \approx \pi$ is evident, which does not exist in a normal-metal Cu-JJ-based SQUID (Fig. 4 and Extended Data Fig. 4). In ferromagnetic spin-triplet JJs[29], whether the JJ will be a 0 junction or a π junction depends on the sum of the rotational chirality from left spin-mixer FM_1 to central spin-rotator FM_2 and that from central spin-rotator FM_2 to right spin-mixer FM_3. If the JJ has the same rotational chirality across the entire $FM_1/FM_2/FM_3$ Josephson barrier, then the junction will be a 0 junction, whereas if it has the opposite rotational chirality across the $FM_1/FM_2/FM_3$ barrier, then the junction will be a π junction. This suggests that the OOP rotational chirality and ground-state phase difference of our chiral antiferromagnetic spin-triplet JJs seem to be controlled by external OOP magnetic fields. In fact, our theoretical modelling (Methods and Supplementary Section 1) assures that both Josephson

https://doi.org/10.1038/s41565-023-01336-z

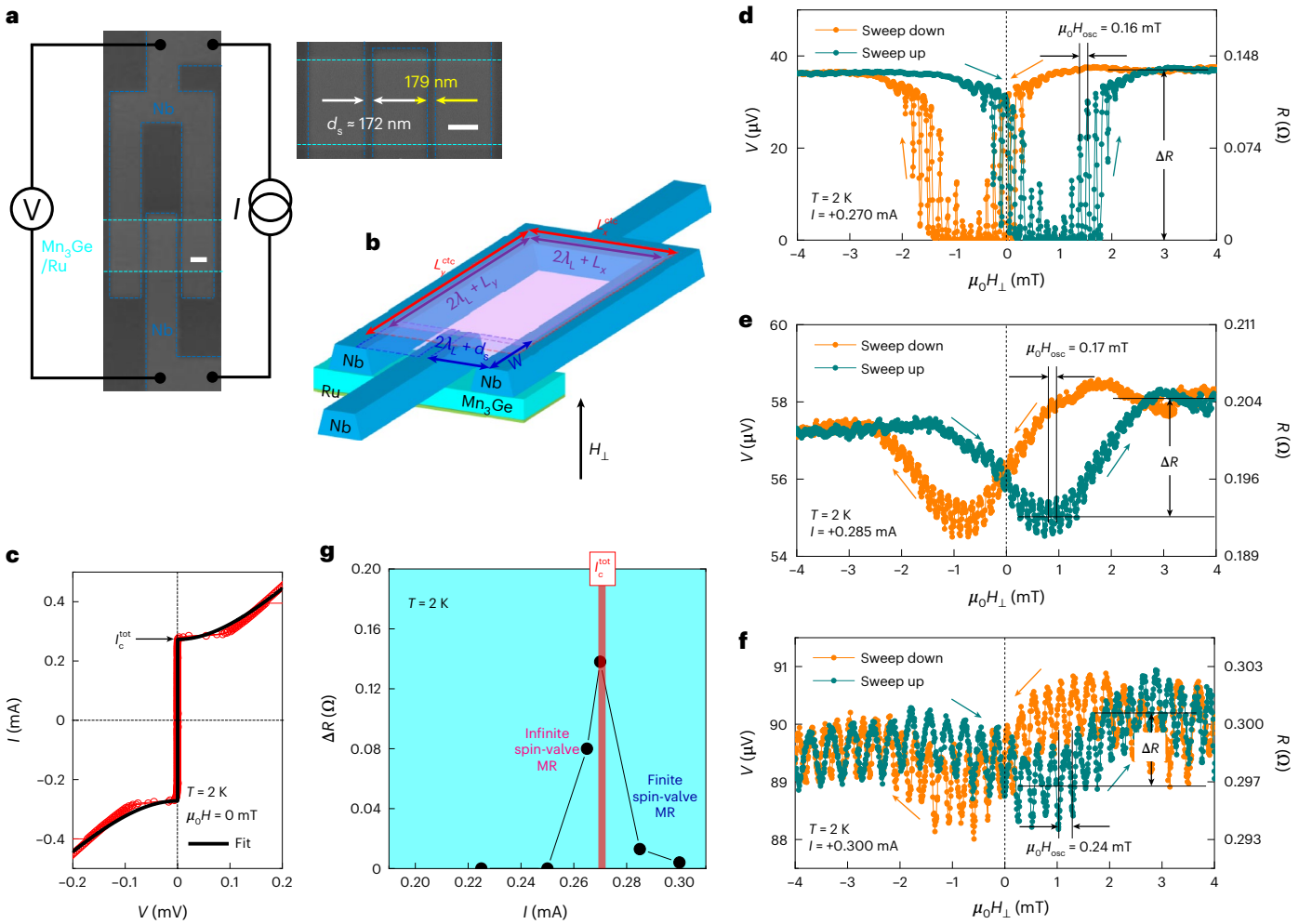

Fig. 3 | Spin-triplet supercurrent spin valve implemented in Mn_3Ge JJ-based SQUID. a,**b**, Scanning electron micrographs (**a**) and measurement scheme (**b**) of the fabricated d.c. SQUID, which contains two Nb/Mn_3Ge/Nb JJs with barrier spacing d_s = 172 and 179 nm ($\geq \xi_{triplet}^{Mn_3Ge}$) that are laterally connected through the single layer of $D0_{19}$-Mn_3Ge(0001). Scale bar, 0.5 μm (**a**). Note that if the width of the SQUID track is much larger than the London penetration depth λ_L, flux focusing effectively widens the SQUID area to be $L_x^{ctc}L_y^{ctc}$, where $L_{x,y}^{ctc}$ is the centre-to-centre spacing between the tracks defining the two opposite sides of the SQUID. Zero-field I–V curve of the Mn_3Ge JJ-based SQUID at T = 2 K. **d**–**f**, Time-averaged voltage V as a function of perpendicular magnetic field $\mu_0H_\perp$ for the I-biased SQUID, taken at T = 2 K. From the periodic $V(\mu_0H_\perp, I \geq I_c^{tot})$ modulation in **d**–**f**, we find a characteristic period of μ_0H_{osc} = 0.16–0.24 mT (Extended Data Fig. 3). **g**, Spin-valve amplitude $\Delta R = R_{high} - R_{low}$, implemented in the SQUID $V(\mu_0H_\perp)$ oscillation versus I. Note that for $I \lesssim I_c^{tot}(\mu_0H_\perp = 0)$, we achieve an infinite spin-valve magnetoresistance $MR = \frac{\Delta R}{R_{low}} \rightarrow \infty$ by definition, indicative of rigorous switching between quasiparticle currents and supercurrents.

critical current and phase shift crucially depend on the chiral antiferromagnetic spin structure (or spin textures in the chiral AFM), which can change when the OOP magnetic field is swept. As presented by equation (23) in Supplementary Section 1, our theory predicts that for $d_s\frac{2JM_0}{\hbar v_F}\tau > \pi/2$, the JJ can transition to a π junction from a 0 junction. Given our theory (equation (28) in Supplementary Section 1) that $\frac{2J\delta M}{\hbar v_F}$ is the inverse decay length of triplet supercurrents $\left(\xi_{triplet}^{Mn_3Ge}\right)^{-1}$ and δM is in the same order as M_0, we theoretically expect the 0-to-π transition appearing for $d_s > \frac{\pi}{2}\left(\frac{\hbar v_F}{2JM_0}\right) \approx \frac{\pi}{2}\xi_{triplet}^{Mn_3Ge} \approx 200$ nm (whose value is taken from Extended Data Fig. 1). This agrees with what we observe (Fig. 3f and Extended Data Fig. 4). We also emphasize that for $d_s \approx 80$ nm ($< \xi_{triplet}^{Mn_3Ge}$) Mn_3Ge JJ-based SQUID (Extended Data Fig. 5), none of the supercurrent spin-valve behaviour and the 0-to-π phase shift as a function of $\mu_0H_\perp$ clearly emerge, which is again consistent with our theoretical prediction (equation (28) in Supplementary Section 1).

By substituting the chiral AFM Mn_3Ge with normal-metal Cu (Fig. 4a,b), we also perform a control experiment to check a possible contribution of OOP Abrikosov vortex nucleation under $\mu_0H_\perp$. The Cu-JJ-based SQUID reveals higher $I_c^{tot}(\mu_0H_\perp = 0)$ even with larger d_s (201 and 205 nm; Fig. 4c) than the Mn_3Ge JJ-based SQUID, as would be expected for the long singlet superconducting proximity effect (a few hundred nanometres) in the highly conductive normal-metal Cu barrier[31]. Its well-defined $I_c^{tot}(\mu_0H_\perp)$ interference pattern in modest fields further supports a good Josephson property (Extended Data Fig. 4). When biasing $I \geq I_c^{tot}(\mu_0H_\perp = 0)$ to the Cu-JJ-based SQUID (Fig. 4d–f), we do not observe any asymmetric hysteretic behaviour in the $V(\mu_0H_\perp)$ curves (Fig. 4g) but do measure the clear $V(\mu_0H_\perp)$ oscillation of μ_0H_{osc} = 0.16–0.17 mT (Extended Data Fig. 3). This result indicates that OOP Abrikosov vortices are unlikely to be the source of the found supercurrent spin-valve behaviour.

Conclusions

Recent theories[21,22] have suggested that the out-of-kagome-plane overall tilting of the triangular non-collinear AFM spin arrangement by a

https://doi.org/10.1038/s41565-023-01336-z

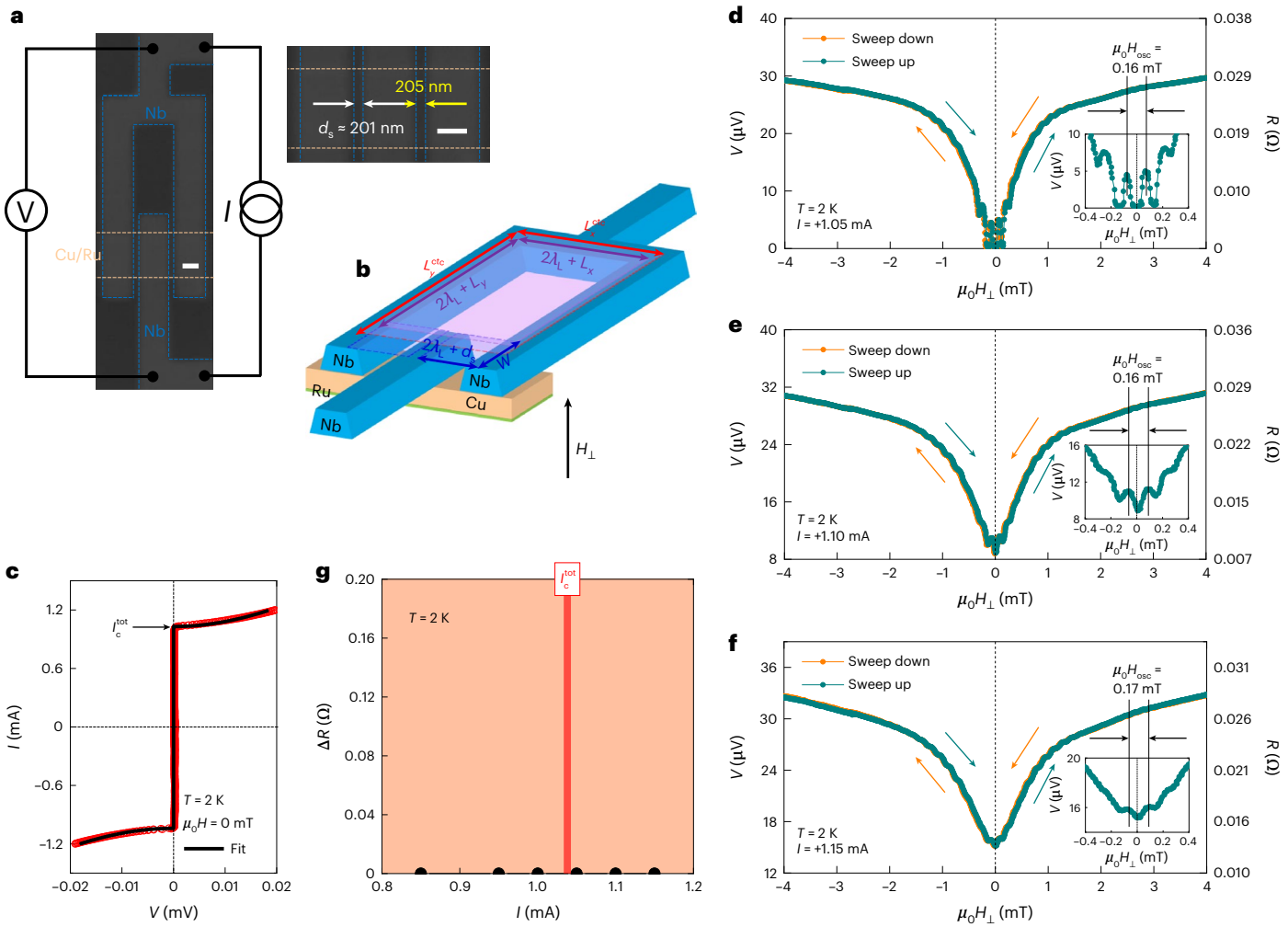

Fig. 4 | Absence of supercurrent spin-valve effect in Cu JJ-based SQUID. **a**–**g**, Data equivalent to Fig. 3a–g but for the d.c. SQUID composed of two Nb/Cu/Nb JJs with longer d_s = 201 and 205 nm, in which the Cu spacer is epitaxial (Extended Data Fig. 2). Scale bar, 0.5 μm (**a**). Note that contrary to the Mn_3Ge JJ-based SQUID, no asymmetric hysteretic response of time-averaged voltage V to perpendicular magnetic field $\mu_0 H_\perp$(≤|3 mT|) is detected in the Cu-JJ-based SQUID (**g**). From the periodic $V(\mu_0 H_\perp,\ I \geq I_c^{tot})$ modulation (insets of **d**–**f**), we find a characteristic period of $\mu_0 H_{osc}$ = 0.16–0.17 mT (Extended Data Fig. 3).

few degrees in Mn_3X (X = Ir, Sn, Ge) indeed visibly changes the k-space Berry curvature near the Fermi energy and the associated anomalous Hall response. In addition, vanishingly small but finite OOP canted magnetization of our $D0_{19}$-Mn_3Ge(0001) film (Extended Data Fig. 6) enables the hysteretic behaviour of Josephson supercurrents as a function of $\mu_0 H_\perp$. These further support our claim that magnetic-field-controlled triplet pairing states through the Berry curvature modification can lead to the spin-triplet supercurrent spin-valve effect even in a single topological chiral AFM. In fact, our theory, which takes both real-space magnetic texture (under an OOP magnetic field) and k-space Weyl nodes into account (Supplementary Section 1), reproduces the observed hysteric Fraunhofer pattern (Fig. 1d). Although the theory has to be further developed, especially regarding full boundary conditions for quasiclassical Green's functions and their chirality dependence, our present model reasonably captures the physics behind our experimental findings (that is, hysteresis in the Fraunhofer pattern and 0-to-π phase shift in the SQUID data). How microscopic details of antiferromagnetic spin texturing and out-of-kagome-plane titling affect the chirality-dependent phase also need to be systematically studied in the future. We believe that our result facilitates a better understanding of the role of the Berry curvature in singlet-to-triplet pair conversion, inspires future theoretical studies on the interplay of Berry curvature and spin-triplet pairing in a chiral non-collinear AFM in more detail and provides a radical route for controlling the triplet-pair amplitude by an extremely small magnetic field—an essential prerequisite for logic circuit[1] or AFM domain-wall sensor[28] applications of spin-triplet supercurrents.

Online content

Any methods, additional references, Nature Portfolio reporting summaries, source data, extended data, supplementary information, acknowledgements, peer review information; details of author contributions and competing interests; and statements of data and code availability are available at https://doi.org/10.1038/s41565-023-01336-z.

References

1. Linder, J. & Robinson, J. W. A. Superconducting spintronics. *Nat. Phys.* **11**, 307–315 (2015).
2. Eschrig, M. Spin-polarized supercurrents for spintronics: a review of current progress. *Rep. Prog. Phys.* **78**, 104501 (2015).
3. Birge, N. O. Spin-triplet supercurrents in Josephson junctions containing strong ferromagnetic materials. *Philos. Trans. R. Soc. A* **376**, 20150150 (2018).
4. Houzet, M. & Buzdin, A. I. Long range triplet Josephson effect through a ferromagnetic trilayer. *Phys. Rev. B* **76**, 060504(R) (2007).

5. Bergeret, F. S., Volkov, A. F. & Efetov, K. B. Long-range proximity effects in superconductor-ferromagnet structures. *Phys. Rev. Lett.* **86**, 4096–4099 (2001).
6. Cottet, A. Inducing odd-frequency triplet superconducting correlations in a normal metal. *Phys. Rev. Lett.* **107**, 177001 (2011).
7. Bergeret, F. S. & Tokatly, I. V. Spin–orbit coupling as a source of long-range triplet proximity effect in superconductor–ferromagnet hybrid structures. *Phys. Rev. B* **89**, 134517 (2014).
8. Robinson, J. W. A., Witt, J. D. S. & Blamire, M. G. Controlled injection of spin-triplet supercurrents into a strong ferromagnet. *Science* **329**, 59–61 (2010).
9. Khaire, T. S., Khasawneh, M. A., Pratt, W. P. Jr. & Birge, N. O. Observation of spin-triplet superconductivity in Co-based Josephson junctions. *Phys. Rev. Lett.* **104**, 137002 (2010).
10. Keizer, R. S. et al. A spin triplet supercurrent through the half-metallic ferromagnet CrO_2. *Nature* **439**, 825–827 (2006).
11. Jeon, K.-R. et al. Enhanced spin pumping into superconductors provides evidence for superconducting pure spin currents. *Nat. Mater.* **17**, 499–503 (2018).
12. Banerjee, N. et al. Controlling the superconducting transition by spin-orbit coupling. *Phys. Rev. B* **97**, 184521 (2018).
13. Banerjee, N., Robinson, J. W. A. & Blamire, M. G. Reversible control of spin-polarized supercurrents in ferromagnetic Josephson junctions. *Nat. Commun.* **5**, 4771 (2014).
14. Martinez, W. M., Pratt, W. P. Jr. & Birge, N. O. Amplitude control of the spin-triplet supercurrent in S/F/S Josephson junctions. *Phys. Rev. Lett.* **116**, 077001 (2016).
15. Nayak, A. K. et al. Large anomalous Hall effect driven by a nonvanishing Berry curvature in the noncolinear antiferromagnet Mn_3Ge. *Sci. Adv.* **2**, e1501870 (2016).
16. Kiyohara, N., Tomita, T. & Nakatsuji, S. Giant anomalous Hall effect in the chiral antiferromagnet Mn_3Ge. *Phys. Rev. Appl.* **5**, 064009 (2016).
17. Soh, J.-R. et al. Ground-state magnetic structure of Mn_3Ge. *Phys. Rev. B* **101**, 140411(R) (2020).
18. Xiao, D., Chang, M.-C. & Niu, Q. Berry phase effects on electronic properties. *Rev. Mod. Phys.* **82**, 1959–2007 (2010).
19. Chen, T. et al. Anomalous transport due to Weyl fermions in the chiral antiferromagnets Mn_3X, X=Sn, Ge. *Nat. Commun.* **12**, 572 (2021).
20. Jeon, K.-R. et al. Long-range supercurrents through a chiral non-collinear antiferromagnet in lateral Josephson junctions. *Nat. Mater.* **20**, 1358–1363 (2021).
21. Chen, H., Niu, Q. & MacDonald, A. H. Anomalous Hall effect arising from noncollinear antiferromagnetism. *Phys. Rev. Lett.* **112**, 017205 (2014).
22. Busch, O., Göbel, B. & Mertig, I. Microscopic origin of the anomalous Hall effect in noncollinear kagome magnets. *Phys. Rev. Research* **2**, 033112 (2020).
23. Fermin, R. et al. Superconducting triplet rim currents in a spin-textured ferromagnetic disk. *Nano Lett.* **22**, 2209–2216 (2022).
24. Bhatia, E. et al. Nanoscale domain wall engineered spin-triplet Josephson junctions and SQUID. *Nano Lett.* **21**, 3092–3097 (2021).
25. Komori, S. et al. Spin-orbit coupling suppression and singlet-state blocking of spin-triplet Cooper pairs. *Sci. Adv.* **7**, eabe0128 (2021).
26. Barone, A. & Paterno, G. *Physics and Applications of the Josephson Effect* 2nd edn (John Wiley & Sons, 1982).
27. Gubin, A. I., Il'in, K. S. & Vitusevich, S. A. Dependence of magnetic penetration depth on the thickness of superconducting Nb thin films. *Phys. Rev. B* **72**, 064503 (2005).
28. Jungwirth, T., Marti, X., Wadley, P. & Wunderlich, J. Antiferromagnetic spintronics. *Nat. Nanotechnol.* **11**, 231–241 (2016).
29. Glick, J. A. et al. Phase control in a spin-triplet SQUID. *Sci. Adv.* **4**, eaat9457 (2018).
30. Guichard, W. et al. Phase sensitive experiments in ferromagnetic-based Josephson junctions. *Phys. Rev. Lett.* **90**, 167001 (2003).
31. Blum, Y., Tsukernik, A., Karpovski, M. & Palevski, A. Oscillations of the superconducting critical current in Nb-Cu-Ni-Cu-Nb junctions. *Phys. Rev. Lett.* **89**, 187004 (2002).

Publisher's note Springer Nature remains neutral with regard to jurisdictional claims in published maps and institutional affiliations.

Open Access This article is licensed under a Creative Commons Attribution 4.0 International License, which permits use, sharing, adaptation, distribution and reproduction in any medium or format, as long as you give appropriate credit to the original author(s) and the source, provide a link to the Creative Commons license, and indicate if changes were made. The images or other third party material in this article are included in the article's Creative Commons license, unless indicated otherwise in a credit line to the material. If material is not included in the article's Creative Commons license and your intended use is not permitted by statutory regulation or exceeds the permitted use, you will need to obtain permission directly from the copyright holder. To view a copy of this license, visit http://creativecommons.org/licenses/by/4.0/.

© The Author(s) 2023

Methods

Sample growth and characterization

Single-phase hexagonal $D0_{19}$-Mn_3Ge(0001) (ref. 20) and Cu thin films were epitaxially grown on a Ru-buffered Al_2O_3(0001) substrate by d.c. magnetron sputtering in an ultrahigh-vacuum system with a base pressure of 1×10^{-9} torr. A 5-nm-thick Ru buffer layer was first sputtered at 450 °C with a sputtering power of 15 W and Ar pressure of 3 mtorr. Subsequently, Mn and Ge were co-deposited from elemental sputter targets on the Ru(0001) buffer layer at 500 °C and Ar pressure of 3 mtorr, where the sputter powers of 31 and 10 W for Mn and Ge, respectively, were used. Note that these growth conditions are essentially the same as those used for our recent study[20]. On the other hand, the epitaxial Cu layer (Extended Data Fig. 2) was sputtered at 27 °C with a sputter power of 15 W and Ar pressure of 3 mtorr. All these single-phase hexagonal $D0_{19}$-Mn_3Ge(0001) (ref. 20) and Cu epitaxial films were capped with a 1-nm-thick AlO_x layer to prevent oxidation. We performed the structural and magnetic characterizations of the prepared thin films using X-ray diffraction and SQUID vibrating-sample magnetometer, respectively. To investigate the Berry-curvature-driven anomalous Hall effect[15–17,20], we also carried out magnetotransport measurements on the unpatterned $D0_{19}$-Mn_3Ge(0001) film in the van der Pauw geometry.

Lithography patterning and device fabrication

As the fabrication procedure of lateral Nb/Mn_3Ge/Nb JJs (Fig. 1b) was previously discussed[20], here we only describe the fabrication steps for the d.c. SQUID (Figs. 3a and 4a). A central track of either $D0_{19}$-Mn_3Ge/Ru (Fig. 3a) or Cu/Ru epitaxial layers (Fig. 4a) with lateral dimensions of $1.5 \times 50.0\ \mu m^2$ was first defined using optical lithography and Ar-ion-beam etching, and then Au (80 nm)/Ru (2 nm) electrical leads and bonding pads were deposited by Ar-ion-beam sputtering. We subsequently defined the SQUID loop with an inner area of $1.0 \times 3.0\ \mu m^2$ (Figs. 3a and 4a), in which two constituent JJs were formed on top of the Mn_3Ge/Ru (Fig. 3a) or Cu/Ru (Fig. 4a) track via electron-beam lithography and lift-off steps. The 50-nm-thick Nb electrodes were grown by Ar-ion-beam sputtering at a pressure of 1.5×10^{-4} mbar and the two constituent JJs are edge-to-edge separated by $\geq \xi_{triplet}^{Mn_3Ge}$ (157–178 nm; Extended Data Fig. 1). For direct metallic electrical contacts, the Al_2O_3 capping layer and Au surface were etched away by an Ar-ion beam before sputtering the Nb electrodes.

Low-temperature transport measurement

We measured the I–V curves of the fabricated JJs (Fig. 1d) and d.c. SQUID (Figs. 3c and 4c) with a four-probe configuration in a Quantum Design physical property measurement system using a Keithley 6221 current source and Keithley 2182A nanovoltmeter. The Josephson critical current I_c and normal-state zero-bias resistance R_n of each JJ (Extended Data Fig. 1) were determined by fitting the measured I–V curves with the standard formula for overdamped junctions[26], namely, $V(I) = \frac{I}{|I|}R_n\sqrt{I^2 - I_c^2}$. We obtained the magnetic-field interference pattern $I_c(\mu_0 H)$ (Fig. 1d,e and Extended Data Fig. 4) by repeating the I–V measurements at $T = 2$ K with varying magnetic fields $\mu_0 H_\perp$, applied perpendicular to the kagome plane of $D0_{19}$-Mn_3Ge(0001), from negative to positive values, and vice versa. We subsequently measured the $V(\mu_0 H_\perp)$ curves for the I-biased JJs (Fig. 2a–d) and d.c. SQUID (Figs. 3d–g and 4d–g) by sweeping $\mu_0 H_\perp$ up and down.

Quasiclassical theory of superconducting proximity effect and spin-triplet supercurrent spin-valve effect

As presented in Supplementary Section 1, we developed the quasiclassical theory of the superconducting proximity effect in a conventional AFM and chiral AFM. We derived the equations describing the propagation of superconducting correlations in the diffusive limit—Usadel equations—that are relevant to the devices studied experimentally here. We found that all the superconducting correlations of spin-unpolarized singlets ($S = 0$) and spin-zero ($S = 1$, $m_s = 0$) and spin-polarized ($S = 1$, $m_s = \pm 1$) triplets are strongly damped by exchange spin-splitting fields in the conventional AFM, leading to a short-ranged proximity effect[25,32,33]. However, in case of chiral AFM, spin-momentum locking along with the Weyl node structure turned out to cause a distinctively different superconducting proximity effect. The spin-momentum locking implies that spin texturing in the chiral AFM plays the role of a vector potential, thereby phase shifting the superconducting order parameter and inducing a φ-junction (or π-junction) behaviour, which is controlled by modulating the chiral antiferromagnetic spin texturing. Note also that the Weyl node structure (directly relevant to the Berry curvature) imposes the existence of spin-triplet correlations inside the chiral AFM (equation (16) in Supplementary Section 1). These correlations are expected to propagate over a long distance (equation (17) in Supplementary Section 1).

When the OOP magnetic field is applied and swept, the amplitude I_{Chiral} and phase $\varphi_{0,Chiral}$ of the Josephson triplet supercurrent through the $d_s > 150$ nm Mn_3Ge barrier can both visibly change because these values scale directly with d_s and are determined by how the antiferromagnetic spin texture of Mn_3Ge is configured (Supplementary Section 1). This is the theoretical insight that reasonably explains all the experimental findings of the present paper. Full details of our quasiclassical theory, which reproduces the hysteretic Fraunhofer pattern (Fig. 1d) and explains the 0-to-π phase shift in the SQUID data (Extended Data Fig. 3a,b), can be found in equations (24)–(28) in Supplementary Section 1.

Data availability

The data used in this Article are available from the corresponding authors upon reasonable request.

References

32. Bell, C. et al. Proximity and Josephson effects in superconductor/antiferromagnetic Nb/γ-$Fe_{50}Mn_{50}$ heterostructures. *Phys. Rev. B* **68**, 144517 (2003).
33. Weides, M., Disch, M., Kohlstedt, H. & Bürgler, D. E. Observation of Josephson coupling through an interlayer of antiferromagnetically ordered chromium. *Phys. Rev. B* **80**, 064508 (2009).
34. Schroder, D. K. *Semiconductor Material and Device Characterization* 2nd edn (Wiley-Blackwell, 1998).

Acknowledgements

This work was supported by the Alexander von Humboldt Foundation and the National Research Foundation (NRF) of Korea (Grant No. 2020R1A5A1016518).

Author contributions

K.-R.J. and S.S.P.P. conceived and designed the experiments with the help of T.K. B.K.H. grew the thin films of the chiral non-collinear AFM Mn_3Ge and normal-metal Cu, and characterized their crystallinity and magnetic properties. H.L.M. and H.H. helped with the structural analysis. K.-R.J. fabricated the lateral JJs and d.c. SQUID with the help of J.-K.K. and carried out the transport measurements with the help from J.-C.J. K.-R.J. performed the data analysis with the help of T.K. A.C. and T.K. developed the quasiclassical theory of superconducting proximity effect in both conventional AFM and chiral AFM systems. K.-R.J., B.K.H., T.K., A.C. and S.S.P.P. wrote the manuscript with input from all the other co-authors.

Funding

Open access funding provided by Max Planck Society.

Competing interests
The authors declare no competing interests.

Additional information
Extended data is available for this paper at https://doi.org/10.1038/s41565-023-01336-z.

Supplementary information The online version contains supplementary material available at https://doi.org/10.1038/s41565-023-01336-z.

Correspondence and requests for materials should be addressed to Kun-Rok Jeon, Audrey Cottet or Stuart S. P. Parkin.

Peer review information *Nature Nanotechnology* thanks the anonymous reviewers for their contribution to the peer review of this work.

Reprints and permissions information is available at www.nature.com/reprints.

https://doi.org/10.1038/s41565-023-01336-z

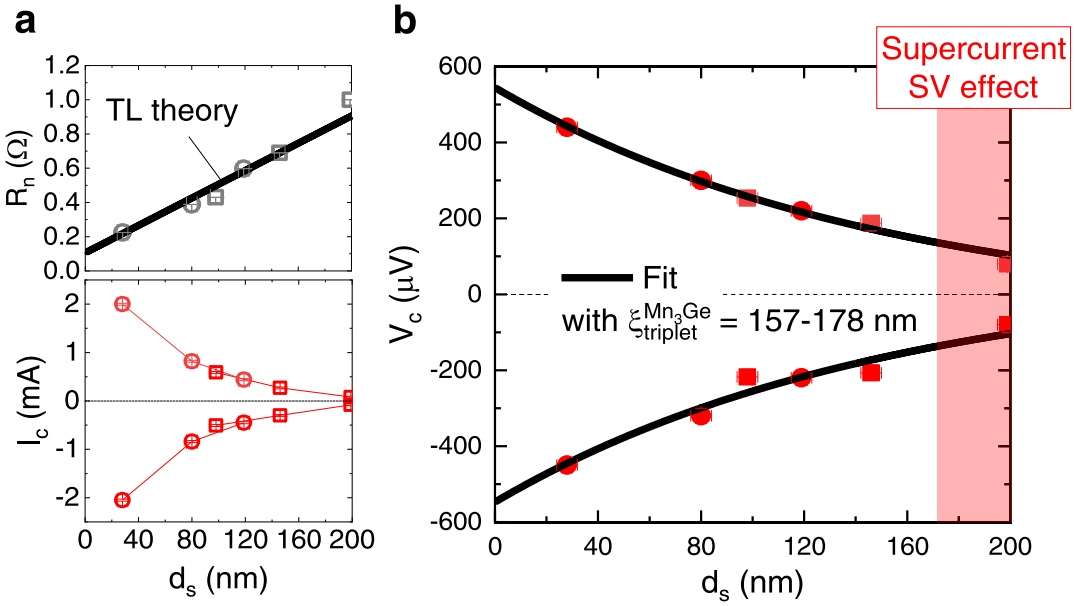

Extended Data Fig. 1 | Long-range supercurrents and spin-valve effect in chiral antiferromagnetic JJs. a, Normal-state zero-bias resistance R_n (top) and Josephson critical current I_c (bottom) of the Nb/Mn_3Ge/Nb JJs versus the barrier spacing d_s. From $R_n(d_s)$ in **a**, we extract the resistance-area product r_i of Nb/Mn_3Ge interfaces to be 1.0–1.2 mΩ μm^2 and the effective resistivity ρ_{ch} for the Mn_3Ge (40 nm)/Ru(5 nm) track to be 25–27 μΩ cm, employing a standard transmission line (TL) theory[34], $R_n = 2R_i + R_{ch} = \frac{\rho_{ch}}{tw}(2l_t + d_s)$. Here $R_i = \frac{r_i}{wl_t}$ and $l_t = \sqrt{\frac{r_i}{\frac{\rho_{ch}}{t}}}$ is the charge transfer length (13 nm). t and w is the thickness and width of the Mn_3Ge/Ru track. **b**, Characteristic voltage $V_c = I_cR_n$ as a function of d_s, from which we determine the decay length $\xi^{Mn_3Ge}_{triplet}$ of the Josephson supercurrents in the Mn_3Ge barrier to be 157–178 nm using an exponential decay function[20], $exp\left(-\frac{\xi^{Mn_3Ge}_{triplet}}{d_s}\right)$ (black curves). Note that for $d_s \geq \xi^{Mn_3Ge}_{triplet}$, the *complete* supercurrent spin-valve effect appears (see Fig. 2d). All I_c values in **a**,**b** are obtained at a fixed temperature $T = 2$ K. Note that data with circle symbols in **a**,**b** are taken from Ref. 20. The error bars in **a** and **b** represent the standard deviation.

https://doi.org/10.1038/s41565-023-01336-z

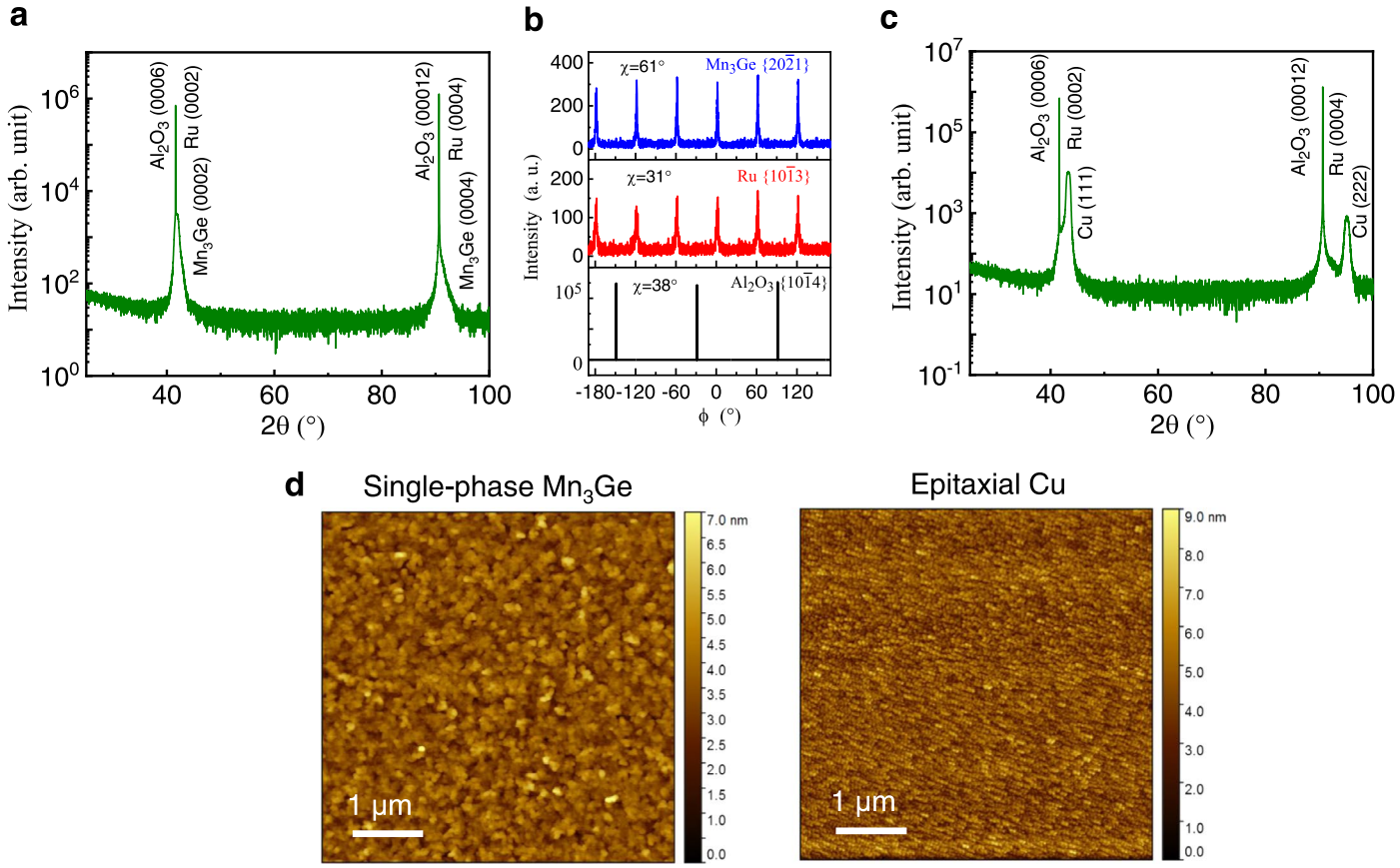

Extended Data Fig. 2 | Structural analysis of the chiral non-collinear AFM Mn_3Ge and the normal-metal Cu. a, Specular θ-2θ XRD pattern of single-crystalline Ru(0001) (black symbol) and single-phase Mn_3Ge(0001)/Ru (red symbol) films grown on Al_2O_3(0001) substrates. **b**, Phi ϕ scan across the Al_2O_3 {10$\bar{1}$4}, Ru {10$\bar{1}$3}, and Mn_3Ge {20$\bar{2}$1} reflections for the same film. **c**, Diffraction pattern of the epitaxial Cu film grown on Ru/Al_2O_3(0001) substrate. **d**, Atomic force micrographs of the single-phase Mn_3Ge(0001) and epitaxial Cu films over 5×5 μm^2 scan area (from left to right respectively). The root-mean-square roughness R_{rms} of the single-phase Mn_3Ge (epitaxial Cu) is estimated to be 0.7 (0.6) nm. These data confirm that the single crystallinity and surface morphology of previous[20] and current $D0_{19}$-Mn_3Ge(0001) films are almost identical.

https://doi.org/10.1038/s41565-023-01336-z

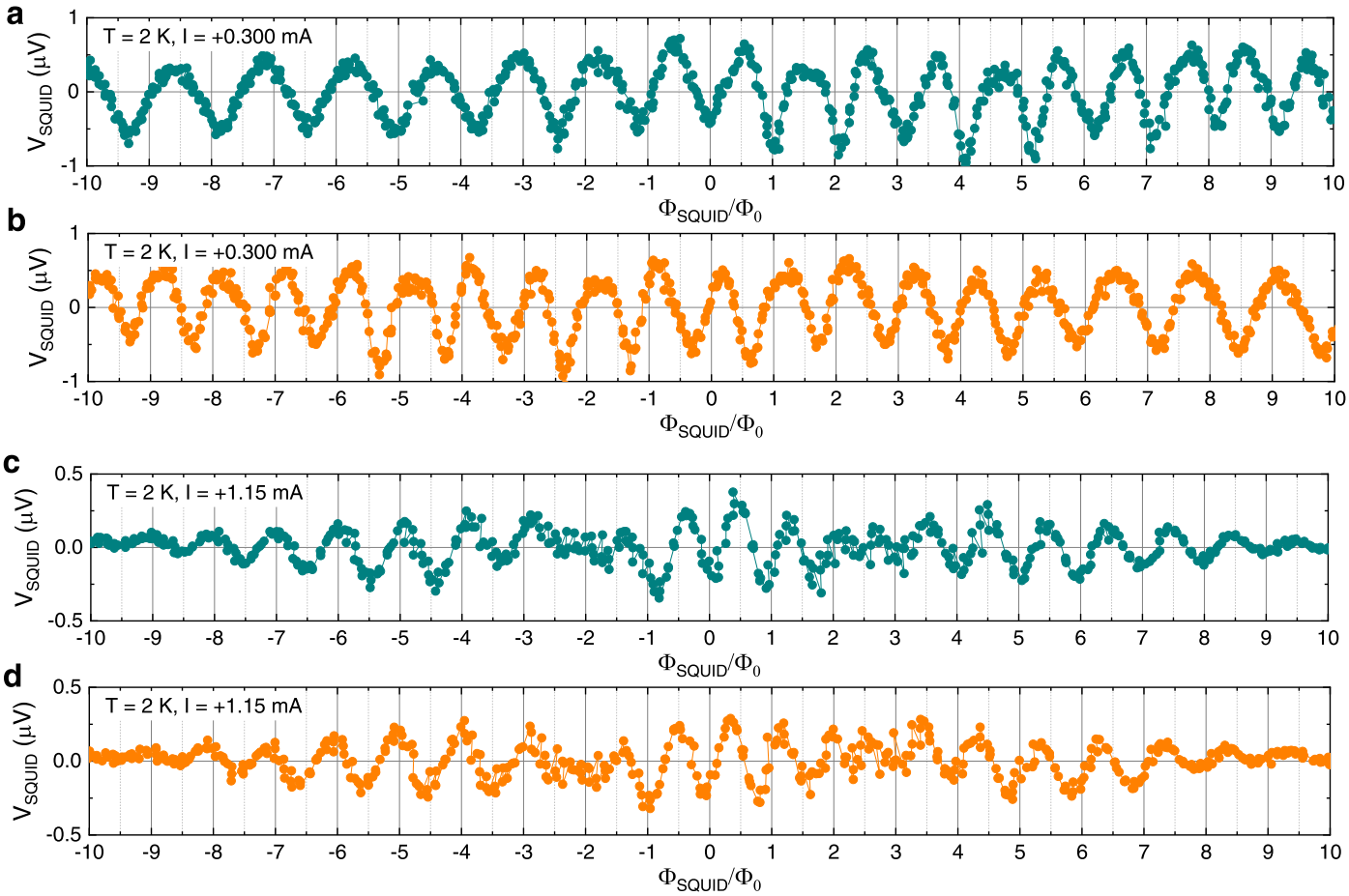

Extended Data Fig. 3 | Magnetic-flux-to-voltage conversion in Mn_3Ge JJ- or Cu JJ-based SQUID. SQUID voltage V_{SQUID} oscillation as a function of normalized magnetic flux Φ_{SQUID}/Φ_0 for the $I = +0.30$ mA-biased Mn_3Ge JJ-based SQUID, taken at $T = 2$ K when sweeping $\mu_0 H_\perp$ up (**a**) and down (**b**). Note that we set $A^{eff}_{SQUID} = 9$ μm and subtract background low-order polynomial and asymmetric voltage signals are from Fig. 3f for clarity. **c**,**d**, Data equivalent to **a**,**b** but for the $I = +1.15$ mA-biased Cu JJ-based SQUID. Here $A^{eff}_{SQUID} = 12$ μm is set and background low-order polynomial voltage signals are subtracted from Fig. 4f. Unlike the Cu JJ-based SQUID, there exists a finite phase shift $\varphi_1 + \varphi_2 \approx \pi$ in the sweep-up and sweep-down V_{SQUID} (Φ_{SQUID}/Φ_0) data of the Mn_3Ge JJ-based SQUID. This implies that the rotational chirality[29] and ground-state phase difference of our chiral antiferromagnetic spin-triplet JJs seems to be controlled by $\mu_0 H$ (see main text for details).

https://doi.org/10.1038/s41565-023-01336-z

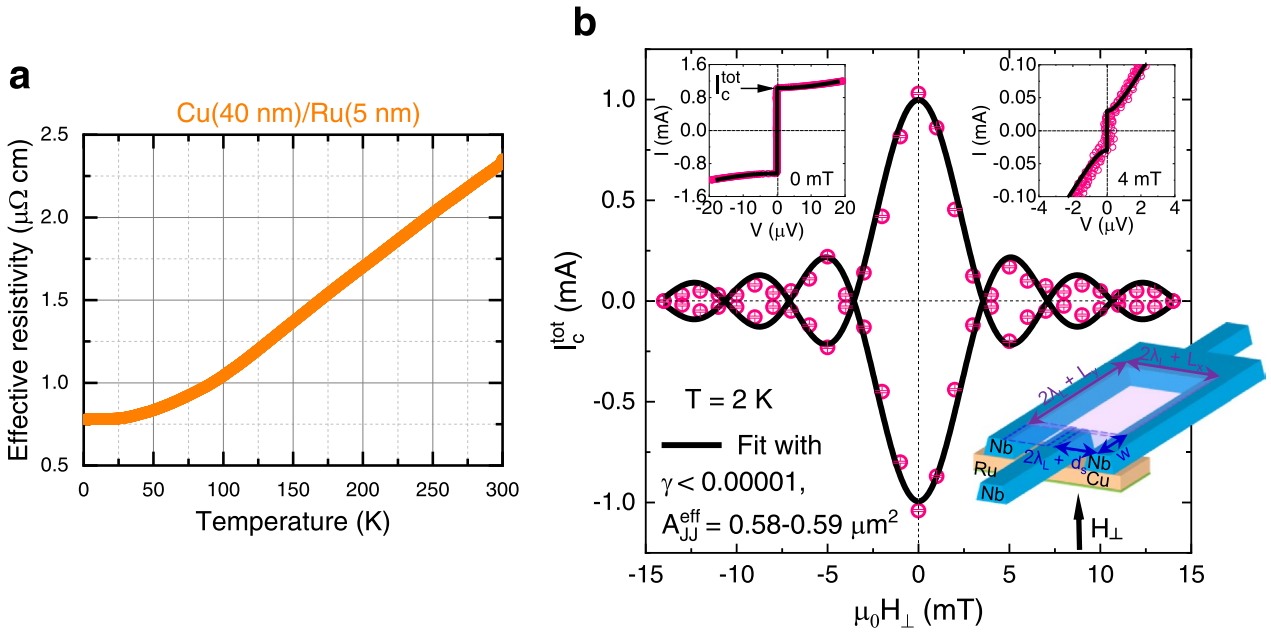

Extended Data Fig. 4 | Magnetic-field interference pattern of the Cu JJ-based SQUID. a, Estimated electrical resistivity versus temperature *T* plot for the Cu (40 nm)/Ru(5 nm) reference Hall-bar device. **b**, Total critical current I_c^{tot} versus $\mu_0 H_\perp$ plot for the Cu JJ-based SQUID, taken at $T = 2$ K. Here $\mu_0 H_\perp$ is applied perpendicular to the interface plane of Nb electrodes, as illustrated in the bottom inset. The top left inset displays the zero-field current-voltage *I-V* curve at 2 K whereas the top right inset shows the *I-V* curve near the zero-order minimum of $I_c^{tot}(\mu_0 H_\perp)$. To focus on a full modulation of I_c^{tot} caused by the magnetic-field quantum interference of two Nb/Cu/Nb lateral JJs, we measure the $I_c^{tot}(\mu_0 H_\perp)$ curves at a rather large interval (1 mT) of $\mu_0 H_\perp$. The black solid lines in **b** are fitting curves[20] to determine the supercurrent non-uniformity γ and the effective junction area A^{eff}_{JJ}. The error bars in **b** represent the standard deviation.

https://doi.org/10.1038/s41565-023-01336-z

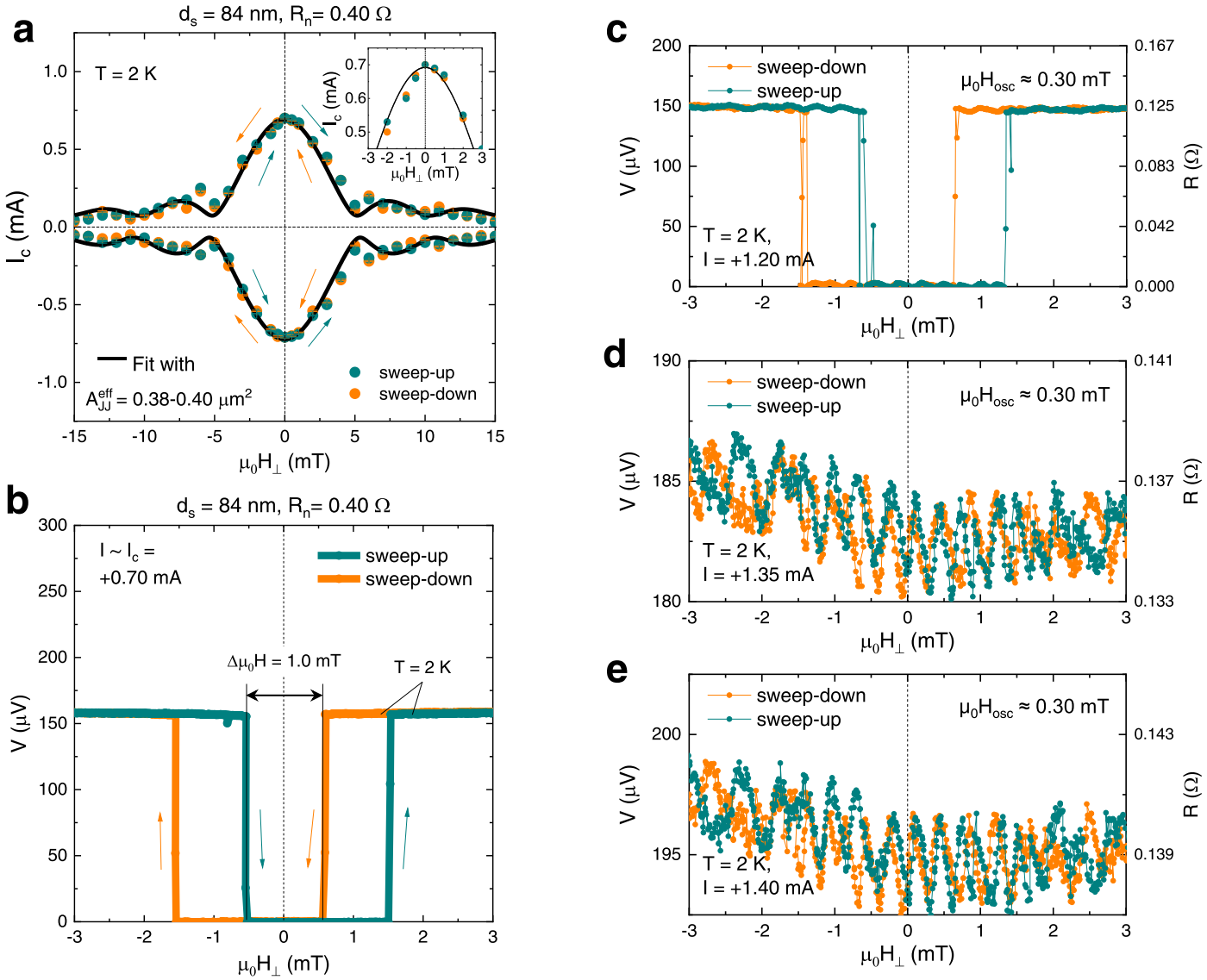

Extended Data Fig. 5 | No supercurrent spin-valve effect and 0-to-π phase shift detectable in the $d_s < \xi^{Mn_3Ge}_{triplet}$ Mn_3Ge JJ-based SQUID. a, Typical magnetic-field interference pattern $I_c(\mu_0 H_\perp)$ of the $d_s = 84$ nm ($<\xi^{Mn_3Ge}_{triplet} = 157$–$178$ nm) JJ. The inset displays the magnified plot around the zero field $\mu_0 H_\perp = 0$. **b**, Time-averaged voltage V as a function of external magnetic field $\mu_0 H_\perp$ for the dc current I-biased $d_s = 84$ nm JJ, taken at 2 K. In this measurement, $\mu_0 H_\perp$ (≤|3 mT|) is applied perpendicular to the Kagome plane of the Mn_3Ge barrier. **c**-**e**, Time-averaged voltage V as a function of perpendicular magnetic field $\mu_0 H_\perp$ for the I-biased SQUID, taken at $T = 2$ K. From the periodic $V(\mu_0 H_\perp,\ I \geq I_c^{tot})$ modulation in **c**-**e**, we find a characteristic period of $\mu_0 H_{osc} \approx 0.30$ mT. None of the supercurrent spin-valve behaviour and the 0-to-π phase shift as a function of $\mu_0 H_\perp$ clearly emerge in the $d_s \approx 80\ nm$ $\left(<\xi^{Mn_3Ge}_{triplet}\right)$$Mn_3Ge$ JJ-based SQUID, which are well consistent with our theoretical modelling [Eq. (S28)]. The error bars in **a** represent the standard deviation.

https://doi.org/10.1038/s41565-023-01336-z

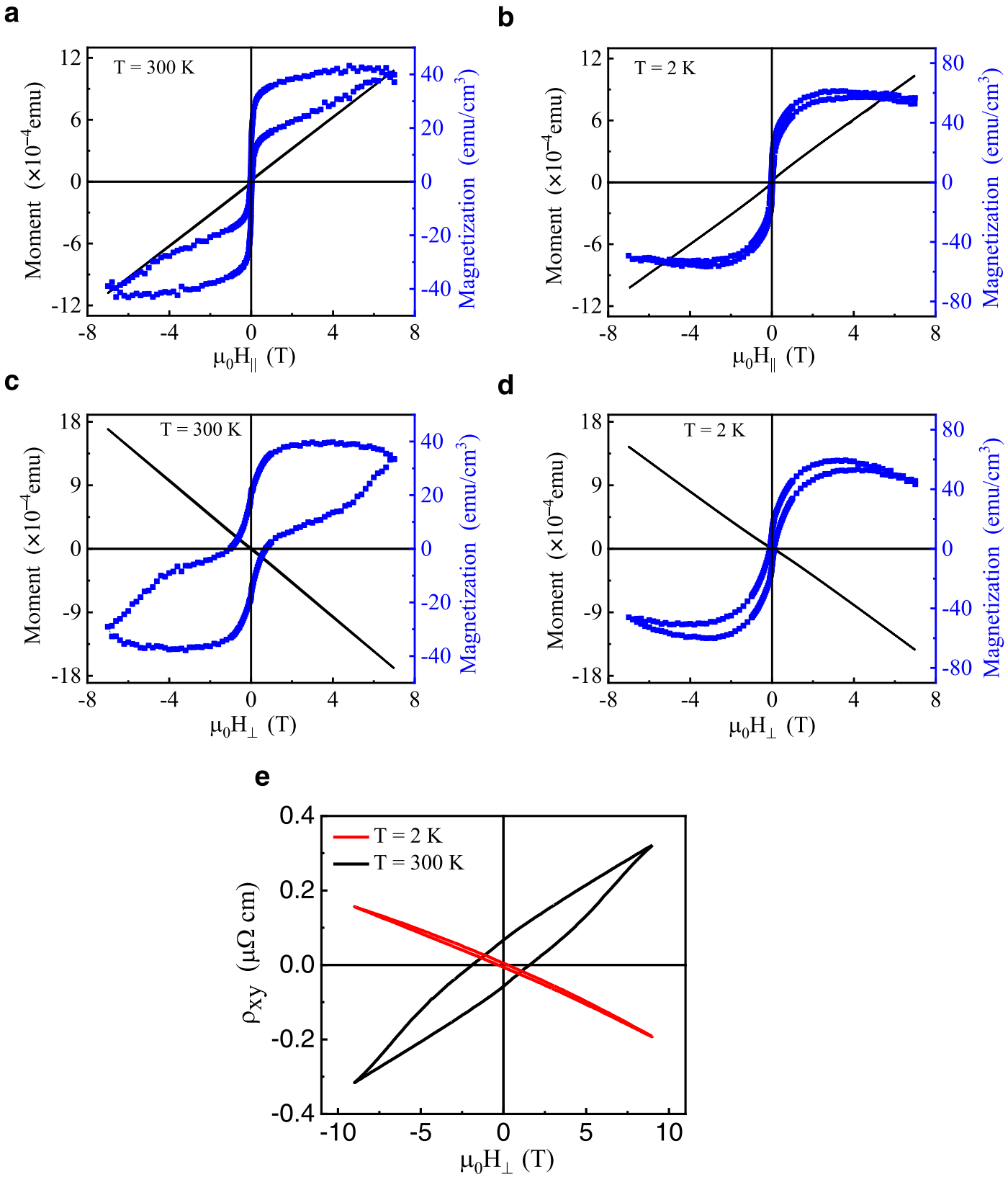

Extended Data Fig. 6 | Magnetic properties and AHE of the chiral non-collinear AFM Mn_3Ge. a,**b**, Typical magnetic hysteresis $M(\mu_0 H_{\parallel})$ curves of the single-phase 40 nm Mn_3Ge(0001) film at 300 K and 2 K, where $\mu_0 H_{\parallel}$ is applied parallel to the Kagome *ab* plane. Black represents the raw measured data and blue represents the corrected data after subtracting the paramagnetic contribution. These data are taken from Ref. 20. **c**,**d**, Data equivalent to **a**,**b** but for the $M(\mu_0 H_{\perp})$ curves, where $\mu_0 H_{\perp}$ is applied perpendicular to the Kagome *ab* plane. **e**, Representative Hall resistivity versus magnetic field *R*-*H* curves of the single-phase Mn_3Ge(0001) at 2 and 300 K. These data, taken from Ref. 20, suggest that there exists vanishingly small but finite OOP canted magnetization of our $D0_{19}$-Mn_3Ge(0001) film, which is in line with the case of bulk Mn_3Ge[15].